REFERENCES AND NOTES

1. For reviews, see R. West, *Angew. Chem. Int. Ed. Engl.* **26**, 1201 (1987); T. Tsumuraya, S. A. Batcheller, S. Masamune, *ibid.* **30**, 902 (1991); G. Raabe and J. Michl, *The Chemistry of Organic Silicon Compounds*, S. Patai and Z. Rappoport, Eds. (Wiley, New York, 1989), part 2, chapt. 17.
2. For reviews, see R. J. P. Corriu and M. Henner, *J. Organomet. Chem.* **74**, 1 (1974); H. Schwarz, *The Chemistry of Organic Silicon Compounds*, S. Patai and Z. Rappoport, Eds. (Wiley, New York, 1989), part 1, chap. 7; J. B. Lambert and W. J. Schulz Jr., *ibid.*, part 2, chap. 16; J. B. Lambert, L. Kania, S. Zhang, *Chem. Rev.* **95**, 1191 (1995); C. Maerker, J. Kapp, P. v. R. Schleyer, *Organosilicon Chemistry: from Molecules to Materials*, N. Auner and J. Weis, Eds. (VCH Press, Weinheim, Germany, 1996), vol. 2.
3. R. West, M. J. Fink, J. Michl, *Science* **214**, 1343 (1981).
4. A. G. Brook, F. Abdesaken, B. Gutekunst, G. Gutekunst, R. K. Kallury, *J. Chem. Soc. Chem. Commun.* **1981**, 191 (1981); A. G. Brook *et al.*, *J. Am. Chem. Soc.* **104**, 5667 (1982).
5. L. Olsson and D. Cremer, *Chem. Phys. Lett.* **215**, 433 (1993); G. A. Olah, G. Rasul, L. Heiliger, J. Bausch, G. K. S. Prakash, *J. Am. Chem. Soc.* **114**, 7737 (1992); M. Kira, T. Hino, H. Sakurai, *ibid.*, p. 6697; P. v. R. Schleyer, P. Buzek, T. Müller, Y. Apeloig, H.-U. Siehl, *Angew. Chem. Int. Ed. Engl.* **32**, 1471 (1993); L. Pauling, *Science* **263**, 983 (1994); G. A. Olah *et al.*, *ibid.*, p. 983; J. B. Lambert and S. Zhang, *ibid.*, p. 984; C. A. Reed and Z. Xie, *ibid.*, p. 985; Z. Xie, R. Bau, C. A. Reed, *J. Chem. Soc. Chem. Commun.* **1994**, 2519 (1994); L. Olsson, C.-H. Ottosson, D. Cremer, *J. Am. Chem. Soc.* **117**, 7460 (1995); G. A. Olah, X.-Y. Li, Q. Wang, G. Rasul, G. K. S. Prakash, *ibid.*, p. 8962; Z. Xie, R. Bau, A. Benesi, C. A. Reed, *Organometallics* **14**, 3933 (1995); G. A. Olah, G. Rasul, H. A. Buchholz, X.-Y. Li, G. K. S. Prakash, *Bull. Soc. Chim. Fr.* **132**, 569 (1995); Z. Xie *et al.*, *J. Am. Chem. Soc.* **118**, 2922 (1996); M. Arshadi, D. Johnels, U. Edlund, C.-H. Ottosson, D. Cremer, *ibid.*, p. 5120.
6. J. B. Lambert, S. Zhang, C. L. Stern, J. C. Huffman, *Science* **260**, 1917 (1993); C. A. Reed, Z. Xie, R. Bau, A. Benesi, *ibid.* **262**, 402 (1993).
7. While our work was in progress, we learned that Lambert and Zhao have synthesized the trimesitylsilylium cation with a ^{29}Si chemical shift at $\delta = 225.5$. We thank them for sending us a preprint (J. B. Lambert and Y. Zhao, *Angew. Chem.*, in press).
8. R. Breslow, *J. Am. Chem. Soc.* **79**, 5318 (1957); ——— and C. Yuan, *ibid.* **80**, 5991 (1958); M. Sundaralingam and L. H. Lensen, *ibid.* **88**, 198 (1966); R. Breslow, *Pure Appl. Chem.* **28**, 111 (1971); A. T. Ku and M. Sundaralingam, *J. Am. Chem. Soc.* **94**, 1688 (1972); F. H. Allen, *Tetrahedron* **38**, 645 (1982); M. W. Wong and L. Radom, *J. Am. Chem. Soc.* **111**, 6976 (1989); W.-K. Li and N. V. Riggs, *J. Mol. Struct.* **89**, 189 (1992).
9. E. D. Jemmis *et al.*, *J. Am. Chem. Soc.* **117**, 11361 (1995).
10. The cyclotrigermene **1** was prepared by reaction of $GeCl_2$-dioxane with $^tBu_3SiNa$ [A. Sekiguchi, H. Yamazaki, C. Kabuto, H. Sakurai, S. Nagase, *J. Am. Chem. Soc.* **117**, 8025 (1995)].
11. Crystals of **1** (20 mg, 0.02 mmol) and trityl tetraphenylborate (20 mg, 0.036 mmol) were put in a glass tube and degassed. Dry oxygen-free benzene was introduced by vacuum transfer and the solution was stirred at room temperature. The solution turned from dark red due to **1** to yellow within 1 min; and the dark brown viscous oil containing **2** separated from the solution. The oily substance was washed with benzene and subsequently with hexane in a glove box to afford air- and moisture-sensitive yellow powders of **2**.
12. The electron transfer reaction followed by cleavage of a Si-Ge bond in **1** may produce the cyclotrigermenium ion **2**, a $^tBu_3Si$ radical, and a Ph_3C radical. However, the details of this reaction are not clear at this moment.
13. Nuclear magnetic resonance (NMR) of **2** ([D_2]dichloromethane solution, 240 K, ^1H) δ values (parts per million): 1.34 (singlet, 81H), ^{t}Bu protons; 6.87 (triplet, 4H, spin-spin coupling constant $J = 7.2$ Hz), aromatic *p*-protons; 7.02 (triplet, 8H, $J = 7.2$ Hz), aromatic *m*-protons; 7.24 – 7.30 (multiplet, 8H), aromatic *o*-protons; NMR of **2** (^{13}C) δ values: 26.6, 31.2, 121.6, 125.7, 135.5, 163.7 (quartet, $^1J_{^{13}C\text{-}^{11}B} = 49$ Hz); NMR of **2** (^{29}Si) δ values: +62.4. The large downfield shift of the ^{29}Si resonances of **2**, relative to those of **1** ($\delta = 37.2$ and 50.1), results from the positive charge of the cyclotrigermenium ion. Ultraviolet spectrum (in dichloromethane solution): λ_{max} (wavelength, maximum of absorption) 276 nm, 350 nm.
14. A yellow-orange crystal (approximate dimensions: 0.30 mm by 0.30 mm by 0.40 mm) of **2** was sealed in a glass capillary and used for x-ray diffraction data collection on a Rigaku Denki AFC-5R diffractometer using a rotating anode (45 kV, 200 mA) with graphite monochromatized Mo K_α radiation ($\lambda = 0.71069$ Å). Cell constants and an orientation matrix for data collection corresponded to the orthorhombic space group $P2_12_12_1$, with $a = 19.10(3)$ Å, $b = 22.84(1)$ Å, $c = 14.84(1)$ Å, and $V = 6475(13)$ Å^3, there are four molecules, $(^tBu_3SiGe)_3{}^+BPh_4{}^-$, per unit cell ($Z = 4$), giving a formula weight of 1135.25, and a calculated density of 1.165 g cm^{-3}. Data were collected at 13° C using the ω-θ scan mode to a maximum 2θ value of 53.0°. From 5154 observed reflections, the structure was solved by direct methods using the applied library program UNICS III system and the RANTAN 81 direct-method program. The structure was refined with all non-hydrogen atoms modelled anisotropically. The H atoms were included in the calculated crystal structure factor F_c, but not refined. The final block-diagonal least squares refinement converged with the unweighted and weighted agreement factors equal to $R = 0.0959$ and $R_w = 0.1027$ for 2797 reflections, with the observed crystal structure factor $F_o > 4\sigma(F_o)$. The large thermal motions of methyl carbon atoms of the ^{t}Bu groups are the main contributing factor to the relatively high *R* factors. Coordinates will be deposited in the Cambridge Crystallographic Database.
15. A cyclotrigallane dianion, $Na_2[(MesC_6H_3)Ga]_3$ (Mes = 2,4,6-trimethylphenyl), has recently been synthesized and shown to be a metallic ring system possessing aromatic character [X.-W. Li, W. T. Pennington, G. H. Robinson, *J. Am. Chem. Soc.* **117**, 7578 (1995); Y. Xie, P. R. Schreiner, H. F. Schaefer III, X.-W. Li, G. H. Robinson, *ibid.* **118**, 10635 (1996)].
16. Aromatic stabilization energies of the D_{3h} $A_3H_3{}^+$ cation are calculated to be 58.7 (A = C), 35.6 (A = Si), 31.9 (A = Ge), 26.4 (A = Sn), and 24.1 (A = Pb) kcal · mol^{-1} (*9*).
17. Electropositive substituents such as silyl groups generally lead to planar Ge=Ge double bonds rather than *trans*-bent structures (*10*). In addition, such electropositive substituents are predicted to reduce the strain within three-membered rings formed by group 14 elements considerably [S. Nagase, *Pure Appl. Chem.* **65**, 675 (1993)].

18. Supported by the Ministry of Education, Science, and Culture of Japan (number 07454159). We also thank ASAI Germanium Research Institute for supplying the tetrachlorogermane.

27 August 1996; accepted 8 November 1996.

Compressibility, Phase Transitions, and Oxygen Migration in Zirconium Tungstate, ZrW_2O_8

J. S. O. Evans, Z. Hu, J. D. Jorgensen, D. N. Argyriou, S. Short, A. W. Sleight*

In situ neutron diffraction experiments show that at pressures above 2 kilobars, cubic zirconium tungstate (ZrW_2O_8) undergoes a quenchable phase transition to an orthorhombic phase, the structure of which has been solved from powder diffraction data. This phase transition can be reversed by heating at 393 kelvin and 1 atmosphere and involves the migration of oxygen atoms in the lattice. The high-pressure phase shows negative thermal expansion from 20 to 300 kelvin. The relative thermal expansion and compressibilities of the cubic and orthorhombic forms can be explained in terms of the "cross-bracing" between polyhedra that occurs as a result of the phase transition.

Materials with a negative coefficient of thermal expansion (either as pure phases or as constituents of composite materials designed to achieve a desired overall coefficient) may become useful in a variety of electronics applications and as substrates for high-precision optical mirrors, components of high-precision thermometers, and catalyst supports. Cubic ZrW_2O_8 was recently shown to exhibit isotropic negative thermal expansion from 0.3 to 1050 K (*1*, *2*). The coefficient of this thermal contraction ($\alpha = -8.8 \times 10^{-6}$ K^{-1}) (*2*) is of the same order of magnitude as that of a so-called high-expansion normal ceramic such as Al_2O_3 ($\alpha = +9 \times 10^{-6}$ K^{-1}) (*3*). The material remains cubic over the entire temperature range, and the contraction is therefore isotropic. In contrast, the low thermal expansion materials currently in use generally expand anisotropically, which can lead to severe problems such as microcracking in ceramics. Further insights into the mechanisms leading to the negative thermal expansion in ZrW_2O_8 may therefore be important both to gain fundamental insight and to design materials.

The structure of ZrW_2O_8 consists of a framework of corner-sharing ZrO_6 octahe-

J. S. O. Evans and A. W. Sleight, Department of Chemistry, Oregon State University, Corvallis, OR 97331, USA. Z. Hu, Intense Pulsed Neutron Source Division, Argonne National Laboratory, Argonne, IL 60439, USA. J. D. Jorgensen and S. Short, Materials Science Division, Argonne National Laboratory, Argonne, IL 60439, USA. D. N. Argyriou, Science and Technology Center for Superconductivity, Argonne National Laboratory, Argonne, IL 60439, USA.

*To whom correspondence should be addressed.

dra and WO_4 tetrahedra in which one oxygen of each WO_4 is "terminal" in nature and is bound to only one W atom. The instability of this structure is revealed by a phase transition at 428 K from acentric to centric cubic that is associated with the onset of considerable mobility of at least one of these terminal O atoms (*1*). The topology of this relatively open framework also gives the structure a high degree of flexibility. Modeling procedures have shown that the connectivity of the lattice can be retained as the cell edge is varied from 8.8 to 9.3 Å (the cubic phase has a cell edge of 9.1575 Å at 293 K and atmospheric pressure), with no distortion of the metal-oxygen bond distances or oxygen-metal-oxygen bond angles of the constituent polyhedra. Instead, the structure can accommodate this artificial change in pressure by a coupled rotation of its constituent polyhedra that requires only changes in the relatively flexible Zr-O-W bond angles (*1*). These studies suggest a model for the negative thermal expansion of ZrW_2O_8 involving thermal libration of these rigid polyhedra and also suggest that ZrW_2O_8 may show unusual properties under applied pressure.

Here we report neutron diffraction data recorded as a function of pressure with the intention of investigating the potential structural flexibility. These experiments have shown, however, that the cubic structure of ZrW_2O_8 becomes unstable at a relatively low pressure (<2 kbar) and undergoes a transition to a related, although structurally distinct, orthorhombic phase. This phase transition gives rise to a ≈5% reduction in cell volume and causes an increase in the average W and O coordination numbers. The new phase remains stable when pressure is released, enabling us to determine its structure and measure both its thermal expansion properties and compressibility. The orthorhombic phase can be converted back to the cubic form by heating at 393 K and ambient pressure. Comparison of the thermal expansivities and compressibilities of both the cubic and orthorhombic forms of ZrW_2O_8, in light of their structural differences, gives support to our model of negative thermal expansion in these materials.

Neutron diffraction data were collected as a function of increasing pressure at room temperature with the use of the Special Environment Powder Diffractometer (SEPD) (*4*) at the Intense Pulsed Neutron Source at Argonne National Laboratory (*5*). As the pressure was increased from 0 to 2 kbar, another crystalline phase appeared (Fig. 1). At 4 kbar, the phase conversion was essentially complete. This phase remained stable after the pressure was released and could be indexed by an orthorhombic unit cell of a = 9.067 Å, b = 27.035 Å, and c = 8.921 Å (*6*, *7*). This unit cell is closely related to that of the cubic material, but with a tripled b axis [a(cubic) = 9.1575 Å at 300 K and room pressure; a(ortho) ≈ c(ortho) ≈ a(cubic), b(ortho) ≈ 3a(cubic)]. The volume change associated with the phase transition is ΔV = −4.98% (*8*).

The structure of the high-pressure phase was solved and refined by powder methods with a combination of laboratory x-ray and high-resolution time-of-flight neutron diffraction data collected after quenching to ambient pressure (Table 1 and Fig. 2) (*9*–*11*). Observed, calculated, and difference profiles from Rietveld refinements using this structural model at various pressures are included in Fig. 1.

The high-pressure orthorhombic form of ZrW_2O_8 (hereafter γ-ZrW_2O_8) is closely related to the low-pressure cubic form at room temperature (α-ZrW_2O_8), although with shifts in metal-atom positions of up to 1 Å and larger oxygen shifts (Fig. 2). The structure of α-ZrW_2O_8 can be described as a corner-sharing framework of ZrO_6 and WO_3 groups, which leads to a framework formula of $ZrW_2O_6^{4+}$. In this formalism, the remaining two oxygen ions are introduced into the structure in either an ordered (<428 K, $P2_13$ in α-ZrW_2O_8) or disordered (>428 K, $Pa\bar{3}$ in β-ZrW_2O_8) fashion. Each of the two crystallographically distinct W atoms is thus tetrahedrally coordinated by four close (distance d ≈ 1.8 Å) O atoms. For each pair of WO_4 tetrahedra (Fig. 2B), there is also a relatively long-

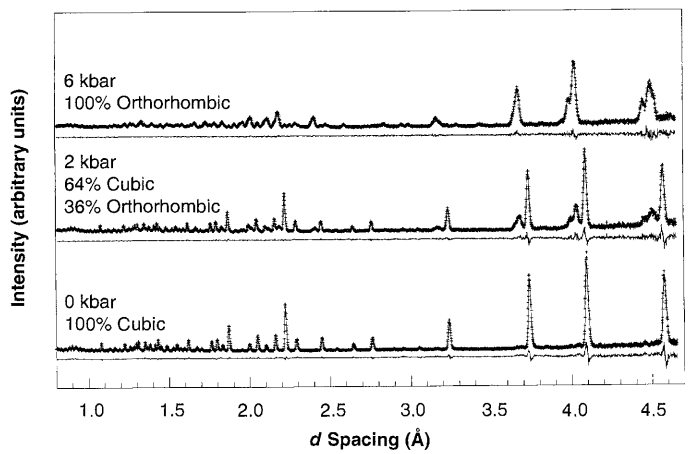

Fig. 1. Time-of-flight neutron diffraction patterns of (bottom) cubic α-ZrW_2O_8 at 300 K and atmospheric pressure, (middle) a 64% α-ZrW_2O_8, 36% γ-ZrW_2O_8 mixture at 2 kbar, and (top) fully converted γ-ZrW_2O_8 at 6 kbar. Observed (+), calculated (solid line), and difference (lower solid trace for each pattern) profiles from Rietveld refinement are shown. Weight percentages of the forms in the mixture were obtained by two-phase Rietveld refinement (*8*).

Table 1. Fractional atomic coordinates from combined x-ray and neutron Rietveld refinement of γ-ZrW_2O_8 at 300 K and atmospheric pressure. Numbers in parentheses are the errors in the last digits. Space group $P2_12_12_1$; a = 9.067 Å, b = 27.035 Å, and c = 8.921 Å. Overall χ^2 = 1.68, wRp(neutron) = 3.84%, wRp(x-ray) = 6.37%, Rp(neutron) = 2.58%, Rp(x-ray) = 4.53%, RF^2(neutron) = 3.29%, and RF^2(x-ray) = 3.04%; number of reflections = 2508 (neutron) and 2655 (x-ray, $K\alpha_1$ and $K\alpha_2$). In addition to fractional atomic coordinates, the cell parameters, histogram scale factors, profile parameters, background terms, and three equated temperature factors were refined (136 parameters total) (*10*). $wRp = \{\Sigma_i^N w_i[y_i(\text{obs}) - y_i(\text{calc})]^2/\Sigma_i^N w_i y_i^2(\text{obs})\}^{1/2}$, $Rp = \{\Sigma_i^N [y_i(\text{obs}) - y_i(\text{calc})]^2/\Sigma_i^N y_i^2(\text{obs})\}^{1/2}$, $RF^2 = \Sigma_i^N |F(\text{obs})^2 - F(\text{calc})^2|/\Sigma_i^N |F(\text{obs})^2|$. $\chi^2 = (wRp/R_{\text{exp}})^2 = \Sigma_i^N w_i[y_i(\text{obs}) - y_i(\text{calc})]^2/(N - P)$; y_i(obs) and y_i(calc) are the observed and calculated intensities at step i, N is the number of observations, and P is the number of parameters.

Atom	x/a	y/b	z/c
Zr1	0.2161(6)	0.4206(2)	0.8080(7)
Zr2	0.7225(7)	0.4239(2)	0.2344(6)
Zr3	0.7438(6)	0.2538(2)	0.7394(7)
W1	0.9021(7)	0.3738(2)	0.5809(6)
W2	0.6276(7)	0.4462(2)	0.8250(6)
W3	0.1395(7)	0.2153(2)	0.8564(6)
W4	0.3786(7)	0.3150(2)	0.6096(6)
W5	0.4053(7)	0.4508(2)	0.4585(6)
W6	0.1279(7)	0.3786(2)	0.2094(6)
O11	0.7104(11)	0.5940(3)	0.9561(10)
O12	0.6541(10)	0.6890(4)	0.1477(10)
O13	0.4974(10)	0.5916(3)	0.2286(10)
O101	0.4599(10)	0.6396(3)	0.9564(10)
O21	0.6929(11)	0.4381(4)	0.0130(10)
O22	0.4395(11)	0.4371(4)	0.8510(10)
O23	0.7050(11)	0.5055(3)	0.7775(10)
O102	0.7883(10)	0.6046(3)	0.2382(10)
O31	0.6705(9)	0.3475(4)	0.1934(11)
O32	0.6910(10)	0.2793(3)	0.9442(10)
O33	0.4544(11)	0.2657(4)	0.1755(10)
O103	0.4455(8)	0.3672(3)	0.5074(11)
O41	0.2302(11)	0.6514(3)	0.2426(10)
O42	0.9593(10)	0.7183(4)	0.1656(10)
O43	0.2230(10)	0.7179(3)	0.9639(10)
O104	0.7693(10)	0.2488(4)	0.2521(10)
O51	0.3531(11)	0.5136(4)	0.3995(11)
O52	0.9833(10)	0.5669(3)	0.7926(9)
O53	0.2417(11)	0.5563(3)	0.1024(10)
O105	0.9480(11)	0.5327(3)	0.0945(11)
O61	0.1865(11)	0.3909(4)	1.0169(10)
O62	0.1602(10)	0.3130(3)	0.2038(10)
O63	0.9360(12)	0.4023(4)	0.1825(12)
O106	0.2625(11)	0.5824(3)	0.8151(8)

range ($d \approx 2.4$ Å) additional interaction between the terminal O atom of one WO_4 group and the adjacent W atom. This leaves, however, one truly one-coordinate O atom for every two WO_4 groups.

In γ-ZrW_2O_8, the basic $ZrW_2O_6^{4+}$ framework remains intact, and there is essentially no change in the ZrO_6 coordination sphere. There are, however, considerable changes in the W coordination environment. The six crystallographically distinct W atoms can be considered as three pairs of WO_4 tetrahedra (W1-W2, W3-W4, and W5-W6) related to those of α-ZrW_2O_8. The 5% reduction in volume can primarily be related to the marked decrease in the W-W distance for groups W1-W2 and W5-W6 [for γ-ZrW_2O_8, d(W1-W2) = 3.84 Å and d(W5-W6) = 3.87 Å; for α-ZrW_2O_8, d(W-W) = 4.16 Å] (Fig. 2). There are two reasons for this decrease. First, there is a significant decrease in the nonbonding W···O distance, leading to an increase in the bonding nature of this interaction. Second, in α-ZrW_2O_8, the WO_4 groups are constrained by symmetry to lie on a threefold axis, and thus their W-$O_{terminal}$ vectors are collinear. At the phase transition, all threefold axes are destroyed, and the W···O-W bond angles can deviate from 180°. This lowering of symmetry, and the resultant tilting of the WO_4 groups, also leads to an increase in W-O bonding interactions because it leads to a significant decrease in distance between the terminal O atom of one pair of WO_4 groups and a W of an adjacent WO_4 pair. For example, this tilting (Fig. 2, C and E) leads to a significant interaction between O105 (the terminal oxygen of the W5-W6 group) and W2 and between O101 (the terminal oxygen of the W1-W2 group) and W6. In the cubic structure, these distances are 3.61 Å; after the phase transition, they are reduced to 2.25 and 2.39 Å, respectively.

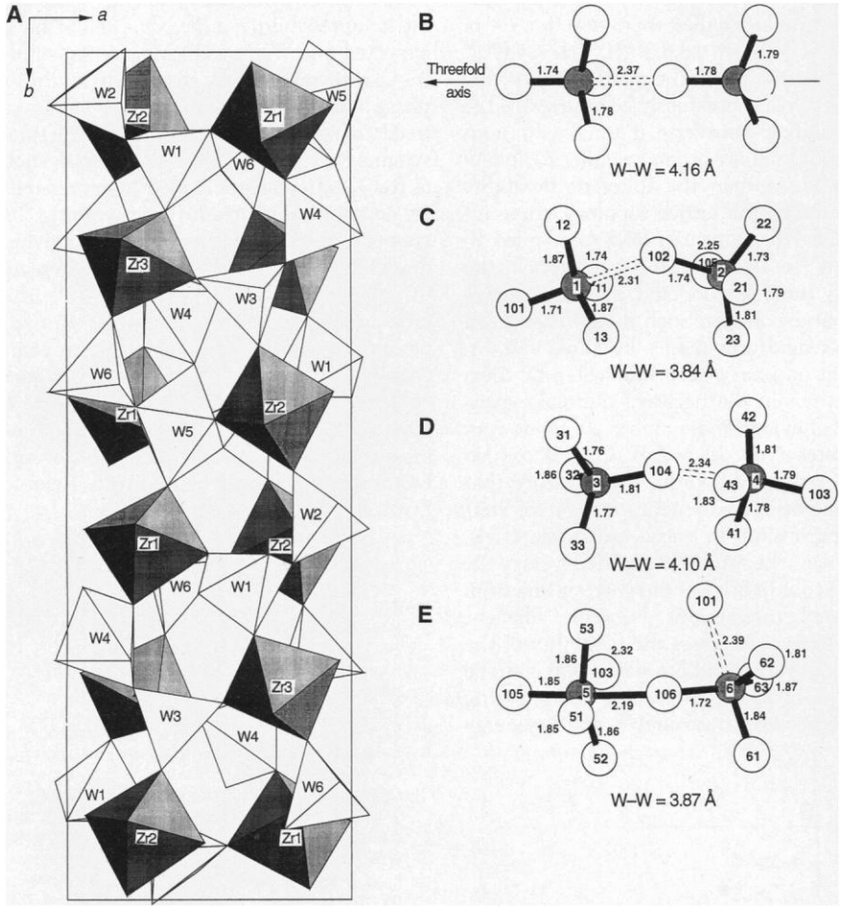

Fig. 2. (**A**) Polyhedral representation of the structure of γ-ZrW_2O_8. The ZrO_6 octahedra are shaded, and the WO_n polyhedra are white. All W-O bond distances less than 2.5 Å have been included in the WO_n polyhedra. (**B**) Schematic representation of the 2(WO_4) groups of α-ZrW_2O_8, viewed perpendicular to the threefold axis. (**C**, **D**, and **E**) Representations of the W coordination environments in γ-ZrW_2O_8. Bond distances are shown in angstroms. Oxygen atoms are white; W atoms are shaded. In each case, bond distances less than 2.3 Å are drawn as solid lines; longer interactions, as dashed lines. Bridging oxygens in the coordination sphere of W*n* (that is, W1 and W2, for example) in the ideal high-symmetry structure are labeled *n*1, *n*2, *n*3; the terminal oxygens are labeled 10*n*. Note the increase in average W coordination number, the "inversion" of the W3-W4 group, and the migration of O103 to W4 and O104 to W3.

Table 2. Cell dimensions as a function of temperature and pressure. Values derived by means of Le Bail fitting of neutron diffraction data (*7*). Estimated standard deviations of 0.0003 Å for *a* and *c* and 0.001 Å for *b* are probably underestimates of the true precision of the measurements.

T (K)	*a* (Å)	*b* (Å)	*c* (Å)	*P* (kbar)	*a* (Å)	*b* (Å)	*c* (Å)
20	9.0748	27.035	8.9191	0.00	9.0680	27.018	8.9120
90	9.0727	27.034	8.9175	1.04	9.0640	27.002	8.9035
160	9.0715	27.031	8.9170	3.11	9.0548	26.977	8.8946
230	9.0710	27.030	8.9166	4.18	9.0487	26.956	8.8911
300	9.0700	27.030	8.9167	5.17	9.0440	26.954	8.8887
				6.23	9.0374	26.937	8.8849

Perhaps the most significant structural change concerns the W3-W4 group. After the phase transition, there is little change in the W3-W4 distance ($d \approx 4.10$ Å), and both W atoms remain approximately tetrahedrally coordinated. There is, however, a change in the orientation of the two tetrahedra. In α-ZrW_2O_8 (and for W1-W2 and W5-W6 of γ-ZrW_2O_8), the WO_4 groups can be considered as having W-$O_{terminal}$ vectors oriented in a definite direction approximately parallel to the original threefold axis of the structure (Fig. 2, B, C, and E). In γ-ZrW_2O_8, the orientation of the W3-W4 tetrahedral pair is reversed (Fig. 2D). This reversal involves the migration of the original terminal O atom of W3 (O103) to W4, and the coupled migration of the terminal O atom of W4 (O104) to W3, bringing the nonbridging O atom of the W3-W4 tungstate groups relatively close to W5 [d(W5-O103) = 2.32 Å]. Thus, the overall coordination number of W5 is increased to 6 (in a pseudo-octahedral arrangement), and perhaps more significantly, that of O103 is increased from 1 to 2.

This oxygen migration is reminiscent of the mechanism proposed to account for the acentric to centric (order-disorder) transition at 428 K in α-ZrW_2O_8 (*1*). In α-ZrW_2O_8, this oxygen-mobility model is supported by significant changes in dielectric properties at the phase transition (*1*). The observation of a similar structural inversion here implies the occurrence of significant oxygen mobility in ZrW_2O_8 at

room temperature and <2 kbar of applied pressure.

The driving forces for this highly unusual phase transition and the implied high oxygen mobility at low temperatures are twofold. First, the transition gives rise to an overall increase in the average W coordination number. In α-ZrW_2O_8, the coordination numbers of the two unique W atoms are best described as 4 and 4+1 (*12*). Of the six crystallographically unique W atoms in γ-ZrW_2O_8, W1, W2, W4, and W6 have 4+1 coordination, W5 has 5+1 coordination, and only W3 remains strictly 4-coordinate (*12*). Perhaps more importantly, for each 2(WO_4) group in α-ZrW_2O_8, there is one O atom that is strictly bonded to only one W atom (the next nearest W being 3.61 Å distant). The bending of W1-W2 and W5-W6 groups and the inversion of the W3-W4 group increases the effective coordination number of all of these terminal O atoms to 1+1. It thus seems likely that the same inherent structural instability that leads to oxygen migration at relatively low temperatures at ambient pressure also drives the pressure-induced transformation to γ-ZrW_2O_8. It is also interesting to speculate on the temperature at which the orthorhombic structure might be induced to form at atmospheric pressure. From the observed temperature dependence of the cell volume of α-ZrW_2O_8 ($V = 773.98 - 0.0214T$ Å^3), α-ZrW_2O_8 would achieve a cell volume per formula unit similar to that of γ-ZrW_2O_8 at around 2100 K. Such a temperature is, however, beyond the stability range of α-ZrW_2O_8.

Neutron diffraction data for γ-ZrW_2O_8 were collected as a function of both temperature and pressure. We found that γ-ZrW_2O_8 retains a negative coefficient of thermal expansion (Fig. 3A and Table 2), with all three axes showing an approximately linear decrease with temperature from 20 to 300 K. The magnitude of this effect ($\alpha_l = -1.0 \times 10^{-6}$ K^{-1}) is an order of magnitude smaller than that for α- or β-ZrW_2O_8 ($\alpha_l = -8.8 \times 10^{-6}$ K^{-1}) (*13*). The negative thermal expansion of α- and β-ZrW_2O_8 has previously been described as the result of transverse thermal vibrations of 2-coordinate O atoms bridging Zr and W atoms (*1*). Given the inherent flexibility conferred by the lattice topology, these individual vibrations can lead to coupled libration of rigid metal-oxygen polyhedra within the structure and overall negative thermal expansion. Such modes have been termed rigid unit modes by Dove and coworkers and have been implicated by them and others in the negative thermal expansion behavior of a number of framework structures (*14*). In γ-ZrW_2O_8, all oxygen atoms remain 2-coordinate, a feature that seems to be a requirement for negative thermal expansion in most oxide materials. However, the increase in the average W and O coordination numbers resulting from increased interactions between adjacent WO_4 groups decreases the flexibility of the structure. These additional bonds can be thought of as "cross-bracing" neighboring polyhedra, and the number of low-energy vibrational modes, which require minimal distortion of the constituent polyhedra or changes in metal-oxygen bond distances, is markedly decreased. This reduction leads to a corresponding decrease in the magnitude of the negative thermal expansion.

The compressibilities of α- and γ-ZrW_2O_8 are 1.44×10^{-3} and 1.47×10^{-3} kbar^{-1}, respectively, at 300 K (Fig. 3B), with all three axes showing comparable compressibilities (*15*). One might have expected γ-ZrW_2O_8 to have a compressibility significantly larger than that of the α phase as a result of the additional degrees of freedom provided by the lower structural symmetry. This is the case in materials such as ReO_3, where the so-called "compressibility collapse" phase transition involving the cooperative tilting of neighboring polyhedra leads to an order of magnitude increase in compressibility (*16*). In γ-ZrW_2O_8, the cross-bracing of neighboring polyhedra apparently prevents such an increase in compressibility. Rietveld refinements on data collected at five pressures between 0 and 6 kbar suggest that the predominant compressibility mechanism of γ-ZrW_2O_8 occurs by means of changes in relatively flexible Zr-O-W bridging units (*17*).

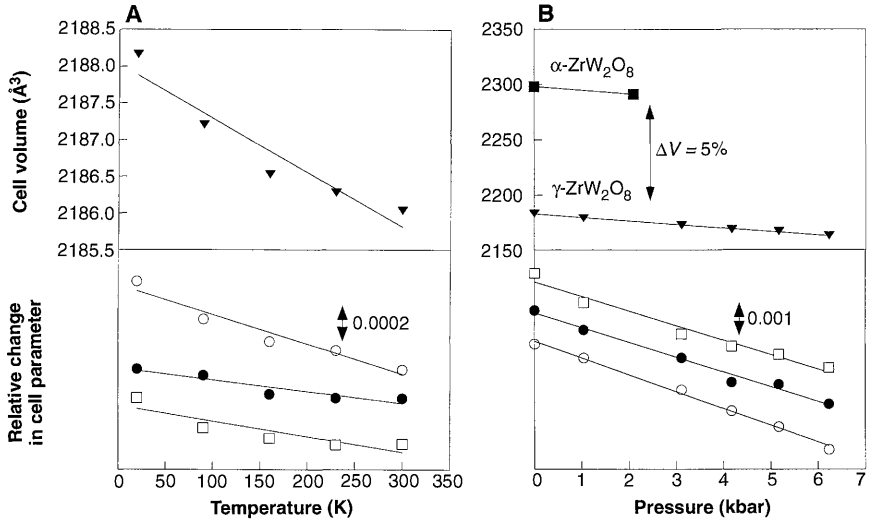

Fig. 3. (**A**) Relative change of unit-cell parameters and cell volume of γ-ZrW_2O_8 over a temperature range of 0 to 300 K. Cell data are plotted as (change in cell parameter)/(cell parameter at 0 K). (**B**) Dependence of the unit-cell parameters of γ-ZrW_2O_8 and the volume of α-ZrW_2O_8 (closed squares) and the volume of γ-ZrW_2O_8 (closed triangles) on applied pressure. Cell data are plotted as (change in cell parameter)/(cell parameter at 0 kbar). Arbitrary *y* axis offsets were used for cell-parameter plots; scale is given by the vertical arrows. Changes in *a* (open circles), *b* (closed circles), and *c* (open squares). Note that the relative magnitudes of the *y* axes for (A) and (B) are different.

REFERENCES AND NOTES

1. T. A. Mary, J. S. O. Evans, T. Vogt, A. W. Sleight, *Science* **272**, 90 (1996); A. W. Sleight, T. A. Mary, J. S. O. Evans, U.S. Patent 5514360 (1995); J. S. O. Evans, T. A. Mary, T. Vogt, M. A. Subramanian, A. W. Sleight, *Chem. Mater.* **8**, 2809 (1996).
2. The coefficient of thermal expansion, defined as $\alpha_l = (l_{T2} - l_{T1})/[l_{T1}(T_2 - T_1)]$, where l is length and T is temperature, was determined by neutron diffraction between 0.3 and 693 K.
3. D. Taylor, *Trans. Br. Ceram. Soc.* **83**, 92 (1984).
4. J. D. Jorgensen *et al.*, *J. Appl. Crystallogr.* **22**, 321 (1989); J. D. Jorgensen *et al.*, *Physica C* **171**, 93 (1990).
5. High-pressure time-of-flight neutron powder diffraction data were recorded in a He gas pressure cell. This cell provided hydrostatic pressure up to 6.5 kbar over the temperature range of 80 to 300 K and allowed pressure and temperature to be varied in situ. The collimation of the cell and the diffraction geometry (90° and 161° fixed-angle scattering) ensured that measurements of diffraction data were free of Bragg scattering from the cell. Diffraction data were obtained for a series of pressures up to 6.2 kbar at 300 K.
6. Cell dimensions were obtained by autoindexing with the program TREOR [J. W. Visser, *J. Appl. Crystallogr.* **2**, 89 (1969)] from x-ray diffraction data. The cell parameters quoted are from Rietveld refinement of the neutron diffraction data recorded in Displex at 300 K.
7. Full pattern fitting by the Le Bail method [A. C. Le Bail, H. Duroy, J. L. Fourquet, *Mater. Res. Bull.* **23**, 447 (1988)] confirmed that all peaks could be indexed on such a cell.
8. At 2 kbar, where both phases are observed simultaneously, the volume change of the transition can be calculated directly. Two-phase Rietveld refinement gave 63.8% cubic (a = 9.140 Å; V = 763.6 Å^3) and 36.2% orthorhombic (a = 9.054, b = 26.988, and c = 8.908 Å; V = 2176.7 Å^3) phase; $\Delta V = -4.98\%$.
9. The x-ray diffraction data for structure solution were collected using Cu Kα radiation on a Siemens D5000 diffractometer between 5° and 60° with a step size of 0.02° and a step time of 10 s. Extinction conditions

suggested space group $P2_12_12_1$. Integrated intensities of 396 reflections were extracted with use of the program EXTRA [A. Altomare *et al.*, *J. Appl. Crystallogr.* **28**, 842 (1995)]. Direct methods in the program SIRPOW [A. Altomare *et al.*, *ibid.* **27**, 435 (1994)] were used to obtain a set of metal coordinates. These coordinates could be approximately related to those of the cubic phase, and initial oxygen positions were inferred from the low-pressure structure. Combined x-ray and neutron Rietveld refinement, initially with metal-oxygen distances heavily restrained to chemically sensible values to prevent divergence, followed by manual shifts of certain O atoms led eventually to a chemically sensible model, in excellent agreement with both x-ray and neutron data. Refinements were performed in the GSAS suite of programs [A. C. Larson and R. B. Von Dreele; Los Alamos National Laboratory (1994)].

10. For final refinement, higher quality diffraction data were used. The x-ray data was collected from 5° to 100° (d_{min} = 1.005 Å) with a step size of 0.02° and a counting time of 45 s per step (4522 data points). Neutron data from SEPD Bank 1, with a time of flight of 6 to 29.5 ms (0.803 to 3.95 Å) and 4699 data points, were used. Because temperature factors refined from powder data are subject to a number of systematic errors, temperature factors were initially set at 0.01 Å^2 for metal atoms and 0.015 Å^2 for O atoms. An absorption correction for neutron data and a surface roughness correction [P. Suortti, *J. Appl. Crystallogr.* **5**, 325 (1972)] for x-ray data were applied. Absorption parameters were then fixed, and equated isotropic temperature factors on individual elements were allowed to refine. On subsequent free refinement of temperature factors, individual values remained within acceptable limits. Impurities of 1.1% WO_3 and 0.8% ZrO_2 were included in the refinement as additional phases.
11. All bond distances and angles lie within normally observed ranges. Bond valences [(*18*); I. D. Brown and D. Altermatt, *Acta Crystallogr. B* **41**, 244 (1985); N. E. Brese and M. O'Keefe, *ibid.* **47**, 192 (1991)] for metal atoms in the structure are chemically reasonable: Zr1, 4.3; Zr2, 4.3; Zr3, 4.4; W1, 6.1; W2, 6.5; W3, 5.6; W4, 5.9; W5, 5.6; and W6, 5.8. The O valences range from 1.8 to 2.2 with only "terminal" oxygens O104 and O105 having slightly low calculated valences (1.6 and 1.7, respectively).
12. There is some question as to what constitutes a true W-O bond in the strictest sense and what is a weaker W···O interaction. We choose here to define a W-O bond as one less than 2.3 Å. Using the valence method of Brown and Wu (*18*), this definition corresponds to interactions contributing greater than 6% of the total valence sum of W being considered as full bonds. A coordination of 4+1 is intended to imply four short (<2.3 Å) and one longer (2.3 to 2.6 Å) interaction.
13. For both cubic and orthorhombic forms, α_i (*2*) is defined as $\frac{1}{3}\alpha_V$, where $\alpha_V = (V_{T2} - V_{T1})/[(T_2 - T_1)V_{T1}]$.
14. A. P. Giddy, M. T. Dove, G. S. Pawley, V. Heine, *Acta Crystallogr. A* **49**, 697 (1993); I. P. Swainson and M. T. Dove, *Phys. Chem. Miner.* **22**, 61 (1995); K. D. Hammonds, M. T. Dove, A. P. Giddy, V. Heine, B. Winkler, *Am. Mineral.* **81**, 1057 (1996); and references therein.
15. Compressibility, defined as $\beta = -(1/V)(dV/dP)$. Linear regression of six cell parameters between 0 and 6 kbar yielded linear compressibilities $-(l_1/l_2)(dl/dP)$ of 0.53 × 10^{-3}, 0.47 × 10^{-3}, and 0.47 × 10^{-3} kbar^{-1} for *a*, *b*, and *c*, respectively.
16. J.-E. Jorgensen, J. D. Jorgensen, B. Batlogg, J. P. Remeika, J. D. Axe, *Phys. Rev. B* **33**, 4793 (1986).
17. Rietveld refinement of high-pressure data was performed with the use of Bank 2 data of SEPD. Time of flight ranged from 4.5 to 26 ms (d = 0.806 to 4.56 Å), yielding 3071 data points. Data at 0, 1.0, 3.1, 5.2, and 6.2 kbar were refined to χ^2/wRp values of 1.1/6.5, 1.5/4.0, 1.4/3.8, 1.5/3.9, and 1.4/3.8%, respectively. Precise determination of individual bond distances and angles for a structure this complex (33 atoms in an asymmetric unit) is difficult given the lower resolution of the data obtained in the high-pressure cell. Average distances: d_{avg}(Zr-O) = 2.069 − (9 × 10^{-4} × P); d_{avg}(W-O) = 1.809 − (2 × 10^{-4} × P); d_{avg}(Zr-W) = 3.80 − (2 × 10^{-4} × P); d_{avg}(W-W) = 3.904 − (3 × 10^{-3} × P) (pressure in kilobars yields distances in angstroms). Average Zr-O-W angle: 160.3 − (0.14 × P).
18. I. D. Brown and K. K. Wu, *Acta Crystallogr. B* **32**, 1957 (1976).
19. The work at Oregon State was supported by NSF (DMR-9308530) and the Oregon Metals Initiative. The work at Argonne National Laboratory was supported by the U.S. Department of Energy [Office of Basic Energy Sciences, Materials Sciences contract U-31-109-ENG-38 (J.D.J., Z.H., S.S.)] and NSF [Office of Science and Technology Centers grant DMR-91-20000 (D.N.A.)].

28 August 1996; accepted 12 November 1996

Disease Extinction and Community Size: Modeling the Persistence of Measles

M. J. Keeling and B. T. Grenfell

A basic issue in ecology is the relation between extinction and population size. One of the clearest manifestations of a population threshold for extinction is the critical community size below which infections like measles do not persist. The current generation of stochastic models overestimates the observed critical community size for measles, generating much less persistence of infection than is observed. The inclusion of a more biologically realistic model for the duration of infection produced a much closer fit to the actual critical community size and explains previously undescribed high-frequency oscillations in measles incidence.

The relation between disease persistence and community size can be explored through the pattern of fadeouts of infection [three or more weeks without reported cases (*1–5*)]. The observed critical community size (CCS) for measles is about 250,000 to 400,000 (Fig. 1A). These figures are based on a large prevaccination data set for 60 towns in England and Wales for the years 1944 to 1968, but they are also typical of the pattern observed for U.S. cities (*2*) and islands (*3*). Below the CCS, the infection often becomes extinct in the troughs between epidemics and must be reintroduced from an external source.

Fadeout pattern predictions from the best current nonspatial stochastic model (*6–13*) significantly overestimate the CCS (Fig. 1A), generating many more fadeouts than observed for towns with populations over 250,000. This discrepancy is even more marked in a comparison of the observed and expected total weeks of fadeout per year (Fig. 1B). Although this standard model [the realistic age-structured (RAS) model (*10–14*)] captures the deterministic dynamics of measles epidemics very well (*5, 10, 13*), its stochastic dynamics are unstable in populations below about 1 million, generating many more fadeouts than observed (*4–6*). A number of authors have sought an explanation for this failure of current models in terms of spatial heterogeneities in transmission, on both large spatial scales (*4, 15–17*) and at the individual (family and school) level (*16*). Although inclusion of spatial heterogeneities reduces the predicted degree of fadeout, even quite complicated spatial models cannot currently capture the low observed level of the CCS (*4, 15–25*).

The fact that the CCS applies to a wide range of communities, from cities to islands, indicates that we should seek a more generic explanation, one rooted in the biology of transmission. We propose that the problem arises because current models are too sensitive to stochastic fluctuations, which arise from the use of long-tailed exponential distributions for the incubation and infectious periods. This exponential formulation arises from the standard assumption that movement from the exposed to the infectious class and then into the recovered class occurs at constant rates a and g, respectively (*6*).

We can modify the standard model to allow for these effects by assuming normal distributions for the incubation and infectious periods (*19*). More complex distributions could be used (*6*), but evidence from the detailed study of transmission in families (*20*) indicates that the periods show limited variation, and the data are well described by infectious periods normally distributed about their means. The use of more discrete periods has been considered previously (*21*) but seldom in this context of seasonally forced stochastic models. The revised stochastic model tends to produce more concentrated pulses of infection, so we will call it the pulsed realistic age-structured (PRAS) model.

Support for the new model is provided by a comparison of Fourier spectra for simulated epidemic time series from the standard (RAS) and modified (PRAS) models with the observed pattern for England and

Department of Zoology, University of Cambridge, Cambridge CB2 3EJ, UK.